Chinese Journal of Catalysis 46 (2023) 48–55

available at www.sciencedirect.com

ScienceDirect

journal homepage: www.sciencedirect.com/journal/chinese-journal-of-catalysis

Article

Dual-atom Co-Fe catalysts for oxygen reduction reaction

Tianmi Tang [a,1], Yin Wang [c,1], Jingyi Han [a], Qiaoqiao Zhang [a], Xue Bai [a], Xiaodi Niu [b,*], Zhenlu Wang [a], Jingqi Guan [a,*]

[a] *Institute of Physical Chemistry, College of Chemistry, Jilin University, Changchun 130021, Jilin, China*
[b] *College of Food Science and Engineering, Jilin University, Changchun 130062, Jilin, China*
[c] *Inner Mongolia Key Laboratory of Carbon Nanomaterials, Nano Innovation Institute (NII), College of Chemistry and Materials Science, Inner Mongolia Minzu University, Tongliao 028000, Inner Mongolia, China*

ARTICLE INFO

Article history:
Received 11 September 2022
Accepted 24 October 2022
Available online 5 March 2023

Keywords:
Dual-atom catalyst
M-N-C
Oxygen reduction reaction
Theoretical calculation
Zn-air battery

ABSTRACT

Controlled synthesis of dual-atom catalysts (DACs) for heterogeneous catalytic reactions is vital but still demanding. Herein, we construct a novel dual-atom catalyst containing FeN_3-CoN_3 sites on N-doped graphene nanosheets (CoFe-NG), which exhibits remarkable catalytic performance with a half-wave potential of 0.952 V for oxygen reduction reaction (ORR) and shows higher endurance to methanol/carbon monoxide poisoning and better durability than commercial Pt/C. The assembled Zn-air battery with CoFe-NG as the air electrode delivers a peak power density of 230 mW cm^{-2} and exhibits negligible change in output voltage at 5 mA cm^{-2} for 250 h. Theoretical calculations reveal that FeN_3-CoN_3 sites on N-doped graphene exhibit lower ORR barrier than FeN_4 and CoN_4 sites, and the rate-limiting step on the former is the transformation of *OH intermediate to H_2O, different from the transformation of *O to *OH on the FeN_4 site and the transformation of O_2 to *OOH on the CoN_4 site.

1. Introduction

Metal-air batteries have been attracting increasing focus owing to their high efficiency, portability, and flexibility for energy demanding devices [1–5]. However, high energy barrier and torpid kinetics of the ORR result in low output power [6,7]. Despite high ORR performance of Pt-based materials, low resistance to CO poisoning and high cost hinders their industrial application. Therefore, developing cost-efficient, high-performance and durable catalysts based on earth-abundant non-noble metals is imperative [8,9]. To modulate the electronic structure of metal sites and increase the ORR activity, many tactics have been proposed, including heteroatom doping, defect engineering, and isolating metal sites [10,11]. Recently, single-atom M-N-C materials have become promising candidates to substitute noble-metal catalysts [12–19].

Both theoretical simulations and experimental results proved that single-atom Fe/Co-N-C catalysts exhibited excellent ORR activity [20]. For Fe-N-C catalysts, FeN_2, FeN_4 and FeN_5 configurations were proposed as the main active sites. For instance, Guo *et al.* [21] revealed that low ORR barrier and fast electron transport can be achieved on FeN_2 sites. Chen *et al.* [22] found that the pyridine nitrogen atom in an additional pyridine ring coordinated to the Fe site in FeN_4 structure could tune the interaction strength of oxygen on the Fe site and in-

* Corresponding author. E-mail: niuxd@jlu.edu.cn (X. Niu), guanjq@jlu.edu.cn (J. Guan).
† Contributed equally to this work.
This work was supported by the National Natural Science Foundation of China (22075099), the Natural Science Foundation of Jilin Province (20220101051JC), and the Education Department of Jilin Province (JJKH20220967KJ, JJKH20220968CY).
https://doi.org/10.1016/S1872-2067(22)64189-5

crease the ORR performance. However, a growing amount of research shows that FeN_4C_x sites might be the efficient centers for the ORR [23]. For Co-N-C catalysts, CoN_4 configuration was generally proposed to be active for the ORR. In 2011, Liu *et al*. [24] annealed cobalt imidazolate framework at 750 °C and adopt acid leaching treatment to obtain a Co-N-C material, which exhibited a half-wave potential ($E_{1/2}$) of 0.68 V in 0.1 mol L^{-1} $HClO_4$. They proposed that the active sites should be CoN_4 configuration. Shao *et al*. [25] discovered that Co-N-C catalysts exhibited better ORR stability than Fe-N-C catalysts due to the lower reaction activity of Co sites for Fenton reactions. However, for monometallic Co-N-C catalysts, the reaction intermediates are adsorbed onto the active sites *via* side-on or end-on patterns, leading to high ORR barriers and the potential attack of M–N bonds [26]. As a contrast, bimetallic single-atom catalysts containing contiguous metal sites with specific synergic action possess great potential to expedite ORR kinetics [27–30]. Bimetallic sites are expected to improve catalytic activity by facilitating O–O bond cleavage *via* a bridge-cis adsorption of ORR intermediates. Additionally, beyond the intrinsic activity, bimetallic sites can improve the durability of M-N-C for the ORR and their practical application potential since it could reduce the attack of M–N bonds by O-containing intermediates during the ORR process [31]. Therefore, in recent years, researchers began to explore the synthesis and electrocatalytic properties of bimetallic single-atom catalysts and found that Fe-Co [31], Fe-Mn [26], Fe-Cu [27], Co-Zn [32], and Co-Pt dual-sites[30] can catalyze the ORR efficiently. To further increase the ORR activity, it is necessary to rationally regulate the diatomic structure and introduce more dual-metal sites.

Here, we employ a facile one-step method to fabricate a highly efficient ORR electrocatalyst with diatomic Co-Fe sites coordinated to nitrogen atoms in graphene framework (CoFe-NG), which exhibits a positive $E_{1/2}$ of 0.952 V *vs*. RHE, far better than single-atom Fe-NG, single-atom Co-NG, and Pt/C catalysts. The CoFe-NG-based Zn-air battery affords a power density of 230 mW cm^{-2} and excellent charge-discharge cycling stability, which can successfully power a small bulb. Theoretical calculations reveal that CoFe-NG possesses lower ORR barrier than Fe-NG and Co-NG, and the rate-limiting step on CoFe-NG is the transformation of absorbed *OH to H_2O, different from the transformation of *O to *OH on the Fe-NG and the transformation of O_2 to *OOH on the Co-NG.

2. Experimental

2.1. Materials preparation

Typically, 100 mg graphene oxide (GO) was decentralized into 50 mL distilled water through ultrasonic treatment for 1 h, and then 2.4 mg $CoCl_2{\cdot}6H_2O$ and 1.4 mg $FeCl_3{\cdot}6H_2O$ were added. After the mixture was stirred for 20 min, the water was removed by lyophilization. Lastly, the obtained precursor was annealed at 750 °C under NH_3 atmosphere or N_2 atmosphere for 2 h, which was nominated as $Co_{0.6}Fe_{0.3}$-NG-750 (simplified as CoFe-NG) or $Co_{0.6}Fe_{0.3}$-G-750 (simplified as CoFe-G), respectively. For comparison, Co-NG, Fe-NG, $Co_{0.6}Fe_n$-NG-750 with different Fe contents (n = 0.1 wt%–0.5 wt%), and $Co_{0.6}Fe_{0.3}$-NG-T annealed at different temperatures (T = 550, 650, 750, and 850 °C) were also synthesized by a similar method to the synthesis of CoFe-NG.

2.2. Characterization

High resolution transmission electron microscopy (HRTEM) was performed on a Philips-FEI Tecnai G2S-Twin microscopy. X-ray diffraction (XRD) was performed on a Shimadzu XRD-6000. X-ray photoelectron spectroscopy (XPS) were recorded on a Thermo Fisher K-alpha. X-ray absorption fine structure (XAFS) spectra of CoFe-NG at Co K-edge and Fe K-edge were performed at the BL14W1 in Shanghai Synchrotron Radiation Facility.

2.3. Electrochemical measurements

ORR tests were conducted on an electrochemical workstation (CHI 760E) coupled with a rotating disk electrode (RDE) system, in which a standard calomel electrode (SCE) and a carbon electrode were served as the reference and counter electrodes, respectively. The potential was standardized into the reversible hydrogen electrode (RHE) according to the equation: $E_{RHE} = E_{SCE} + 0.241V + 0.0591 \times pH$. The number of electron transfer (n) is determined by the slope of the line according to the K-L equation [33].

2.4. DFT calculations

Vienna ab initio simulation package (VASP) was employed for the density functional theory (DFT) calculations [34,35]. The exchange-correlation functional was performed using the projector-augmented wave (PAW) method and Perdew-Burke-Ernzerhof (PBE) potential. The Brillouin zone consists of 2 × 2 × 2 Monkhorst-Pack mesh points. The Nørskov's model was used to explore the ORR mechanism.

3. Results and discussion

3.1. Synthesis and characterization of CoFe-NG

Single-atom Fe-NG, Co-NG, CoFe-NG, and CoFe-G catalysts were synthesized by annealing the mixture of Fe^{3+}/Co^{2+}/graphene oxide under NH_3 and N_2 atmosphere, respectively (Fig. 1(a)). The typical nanosheet morphology of the as-prepared CoFe-NG was confirmed by transmission electron microscope (TEM) image (Fig. 1(b)). Moreover, no obvious metal/metal oxide species can be seen on the graphene nanosheets. From XRD patterns (Fig. S1), no peaks due to metal or metal oxide nanoparticles can be observed in the Fe-NG, Co-NG, CoFe-G, and CoFe-NG, indicating excellent distribution of metal species on the graphene-based supports of these samples. The high-angle-annular dark field scanning transmission electron microscopy (HAADF-STEM) image reveals that the metal ions are atomically distributed in the CoFe-NG nanosheets (Fig. 1(c)). Moreover, both single atoms and dual

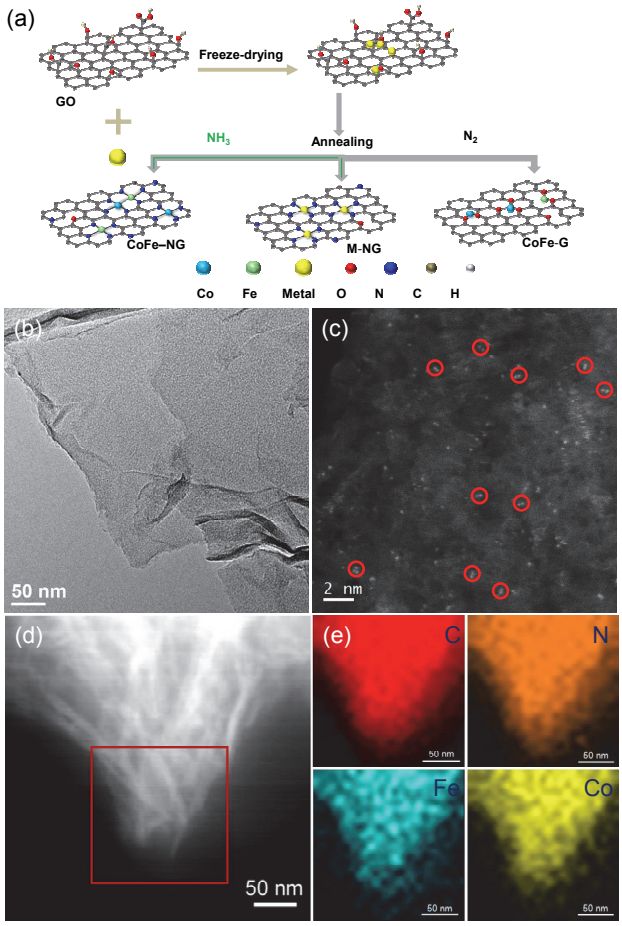

Fig. 1. (a) Illustration of the preparation procedures of CoFe-G, Co/Fe-NG, and CoFe-NG. (b) TEM image of CoFe-NG. (c) Atomic-resolution HAADF-STEM image of CoFe-NG. (d) STEM image of CoFe-NG. (e) EDS elemental mapping images of CoFe-NG.

single-atoms (highlighted by red circles) exist in the CoFe-NG, and the dual single-atom pairs account for ~50% among all the discernible lightspots. The good distribution of C, N, Fe and Co elements in the CoFe-NG is confirmed by STEM elemental mapping (Figs. 1(d) and 1(e)). The loading amounts of Co and Fe are measured to ca. 1.13 wt% and 0.54 wt% in the CoFe-NG, respectively.

The surface compositions of Fe, Co and N species in CoFe-NG were analyzed by XPS (Fig. 2). The two peaks at 711.0 and 724.5 eV in Fe 2*p* XPS spectrum are attributed to Fe^{2+} $2p_{3/2}$ and Fe^{2+} $2p_{1/2}$ (Fig. 2(b)). The two peaks at 781.5 and 786.1 eV in Co 2*p* XPS spectrum are attributed to Co^{2+} $2p_{3/2}$ and Co^{2+} $2p_{1/2}$ (Fig. 2(c)). The N 1*s* XPS spectrum confirms the existence of five different nitrogen species, containing pyridinic nitrogen, metal-nitrogen, pyrrolic nitrogen, graphitic nitrogen and oxidized nitrogen (Fig. 2(d)) [36,37]. X-ray absorption spectroscopy (XAS) was further employed to recognize the chemical nature and structure of Fe and Co species at the atomic scale (Fig. 3). Fig. 3(a) displays the K-edge XANES spectrum of CoFe-NG, FePc, Fe_2O_3 and Fe foil. The position of the white line for CoFe-NG indicates that the oxidation state of the Fe atom is between 0 and +3 and is close to +2. The EXAFS spectrum of CoFe-NG demonstrates a strong peak near 1.40 Å, due to Fe-N path, and a weak peak near 2.67 Å, corresponding to Fe-Co path (Fig. 3(b)). The fitting results show that the length of Fe–N bond is ca. 2.05±0.02 Å and the length of Fe–Co bond is ca. 2.21±0.03 Å (Fig. 3(c)). Fig. 3(d) demonstrates the Co K-edge XANES spectra of Co foil, CoPc, CoO, Co_3O_4 and CoFe-NG. The absorption edge of CoFe-NG is situated between the Co foil and Co_3O_4, indicating the oxidation valence state of the Co atom is higher than metallic Co^0 and lower than Co^{3+} and is close to +2. The EXAFS spectrum of CoFe-NG demonstrates a strong peak near 1.45 Å, ascribe to Co-N path, and a weak peak near 2.67 Å, due to Fe-Co path (Fig. 3(e)). The fitting results show that the length of Co–N bond is ca. 1.90±0.03 Å (Fig. 3(f)).

3.2. *Electrocatalytic ORR performance*

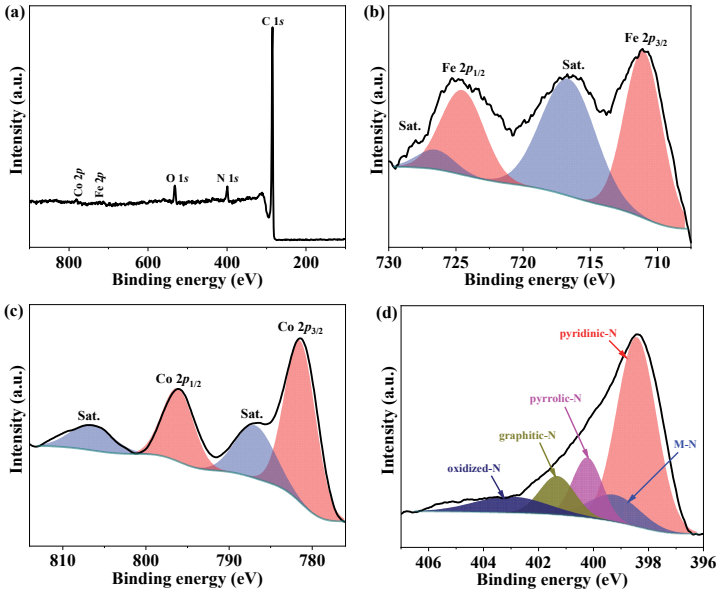

Fig. 2. (a) XPS survey spectrum of the CoFe-NG. (b) Fe 2*p* XPS spectrum. (c) Co 2*p* XPS spectrum. (d) N 1*s* XPS spectrum.

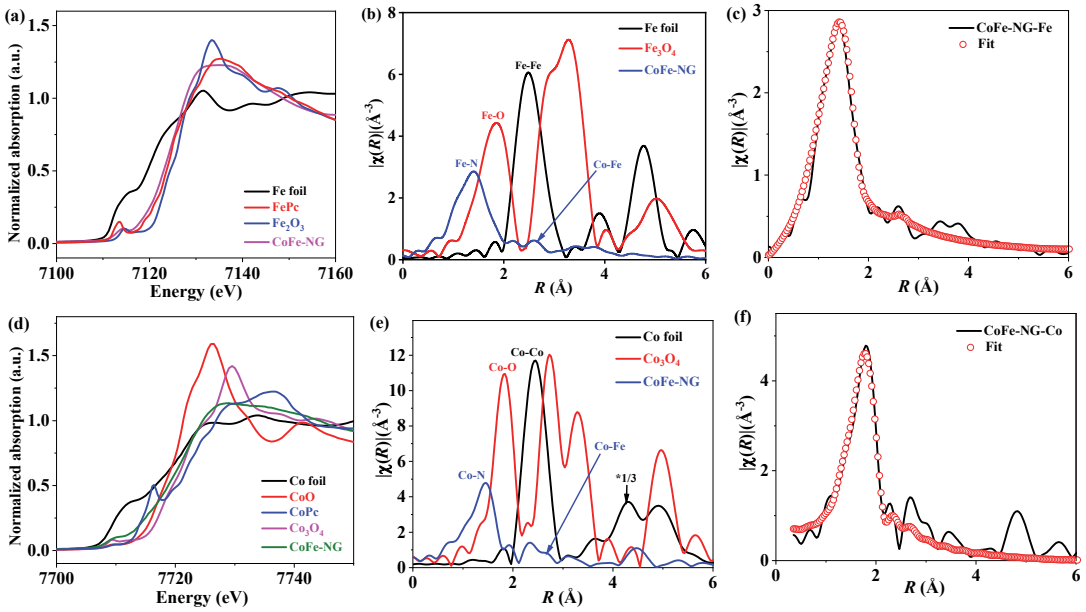

Fig. 3. (a) Fe XANES spectra. (b) Fe EXAFS spectra of CoFe-NG, Fe_3O_4, and Fe foil. (c) FT-EXAFS fitting spectrum at Fe K-edge of CoFe-NG. (d) Co XANES spectra. (e) Co EXAFS spectra of CoFe-NG, Co_3O_4, and Co foil. (f) FT-EXAFS fitting spectrum at Co K-edge of CoFe-NG.

The electrocatalytic ORR activities over the Fe-NG, Co-NG, CoFe-G, CoFe-NG, and commercial 20% Pt/C catalysts were studied using cyclic voltammograms (CVs) (Fig. S2). As observed, the CoFe-NG displays a more positive peak than the Fe-NG, Co-NG, CoFe-G and 20% Pt/C, suggesting higher ORR activity of the CoFe-NG. To further study the ORR prformance, linear sweep voltammetry (LSV) curves were collected (Fig. 4(a)). The $E_{1/2}$ for the CoFe-NG is 0.952 V *vs.* RHE, more positive than Fe-NG (0.872 V), Co-NG (0.857 V), CoFe-G (0.768 V), 20% Pt/C (0.842 V), and most of single-atom catalysts reported previously (Table S1), revealing remarkably enhanced electrocatalytic ORR activity of the CoFe-NG. Moreover, the Tafel slopes derived from the LSV curves using Koutecky-Levich analysis exhibit that the Tafel slope for the CoFe-NG is 46 mV dec^{-1}, much smaller those that for the Fe-NG (82 mV dec^{-1}), Co-NG (56 mV dec^{-1}), CoFe-G (96 mV dec^{-1}), and Pt/C (59 mV dec^{-1}), confirming the excellent activity of the CoFe-NG (Fig. 4(b)). Available active sites involved in the ORR can be evaluated by electrochemically active surface area (ECSA). As exhibited in Figs. S3–S6, the ECSA for CoFe-NG is 432.4 cm^2, larger than that for Fe-NG (181.4 cm^2), Co-NG (208.1 cm^2), and CoFe-NG (181.8 cm^2), implying more efficient active sites in the CoFe-NG for the ORR. The effect of annealing temperature and Fe-doping content on the ORR activity of CoFe-NG was studied. As shown in Fig. S7, the optimum annealing temperature is about 750 °C, which might be beneficial to the formation of

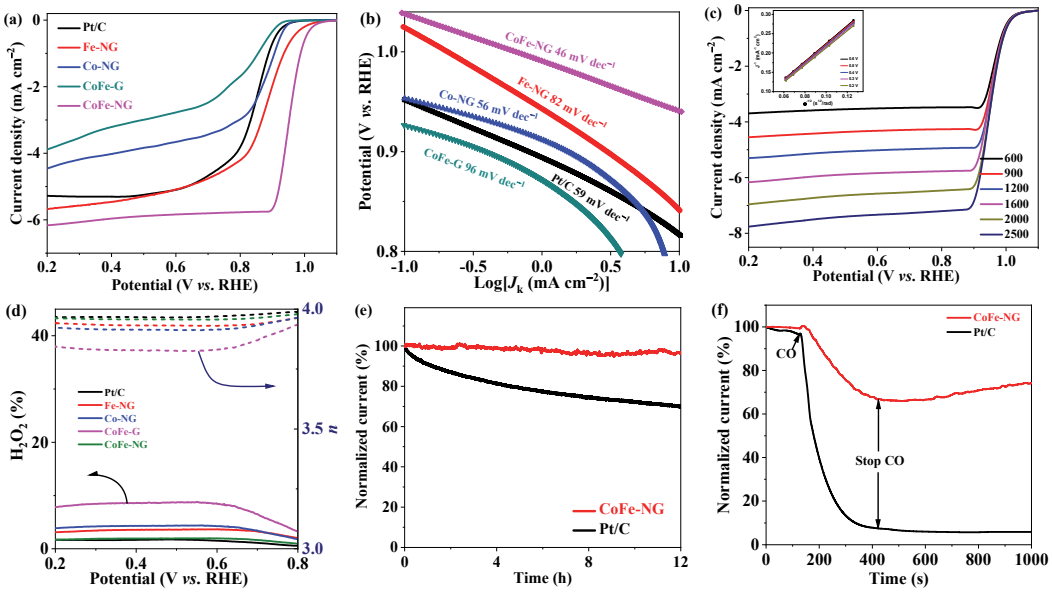

Fig. 4. (a) ORR polarization curves. (b) Tafel slopes. (c) LSV curves of CoFe-NG at different rotation speeds. The inset is the K-L plots. (d) H_2O_2 yield (left) and electron transfer number (n) (right) *vs.* potential for CoFe-NG, CoFe-G, Fe-NG, Co-NG and Pt/C. (e) Chronoamperometry tests of CoFe-NG and 20% Pt/C. (f) Tolerance to CO of CoFe-NG and Pt/C at 0.5 V *vs.* RHE.

dual-atom Co-Fe active sites with appropriate nitrogen coordination configuration [31,38]. The Fe-doping content has a significant impact on the ORR performance of CoFe-NG catalyst (Fig. S8). The experimental results reveal that moderate amount of Fe-doping favors high dispersion of metal species, while excessive Fe-doping might lead to the agglomeration of metal species, thus reducing active sites and lowering ORR activity.

Koutecky-Levich plots (Fig. 4(c), inset) show nearly collateral fitting lines, indicating the first-order ORR kinetics of CoFe-NG [39]. The calculated electron transfer number of CoFe-NG is 3.93–4.0, suggesting a four-electron ORR process. As shown in Fig. 4(d), from 0.2 to 0.8 V, the electron transfer number for the CoFe-NG is in the range of 3.96–4.0 and the H_2O_2 yield remained below 2%, further revealing a high efficiency four-electron ORR process on the CoFe-NG. Compared with Fe-NG, Co-NG, and CoFe-G, CoFe-NG not only exhibits a higher current density but also is more selective for oxygen reduction to OH^-, rather than peroxide (Fig. 4(d)). The chronoamperometry at 0.8 V *vs.* RHE of CoFe-NG shows that the ORR current remains 96.6% after 12 h test, far better than that (70%) of Pt/C (Fig. 4(e)). The carbon monoxide poisoning test was performed by introducing carbon monoxide (flow rate: 50 mL s^{-1}) into the electrolyte (Fig. 4(f)). The slight increase in the current for the CoFe-NG might be due to the interference of current signal after initially introducing carbon monoxide gas. Obviously, the CoFe-NG shows much better endurance to CO poisoning than Pt/C. Moreover, the methanol tolerance of CoFe-NG was evaluated by injecting methanol during the chronoamperometric test (Fig. S9), indicating that the CoFe-NG shows better methanol tolerance than Pt/C. To assess the role of metal ions in the ORR, we performed KSCN poisoning experiment. After introducing 10 mmol L^{-1} KSCN into the KOH solution (Fig. S10), the ORR performances on Fe-NG, Co-NG, CoFe-G and CoFe-NG decrease greatly, implying that SCN^- ions should coordinate strongly with Fe and Co sites and make these sites poisoning. The structure of CoFe-NG after ORR test was characterized by XRD (Fig. S11), which demonstrates that no peaks owing to Fe/Co-based nanoparticles can be notably observed. Moreover, we performed TEM image to see whether the single atoms aggregated after the stability test. As illustrated in Fig. S12, no obvious nanoparticles can be seen, indicating that the single atoms did not aggregate during the ORR. In addition, the valence state of Fe and Co in the CoFe-NG after ORR test was analyzed by XPS (Fig. S13). Partial Fe^{2+} and Co^{2+} ions were oxidized to high valence state Fe^{3+} and Co^{3+} during the ORR process, implying that both Fe and Co sites are involved in the ORR [40,41].

3.3. Zinc-air battery performance

When the CoFe-NG catalyst as an air-cathode catalyst was assembled into a homemade zinc-air battery (ZAB), it can afford an open-circuit voltage of 1.47 V and a high power density

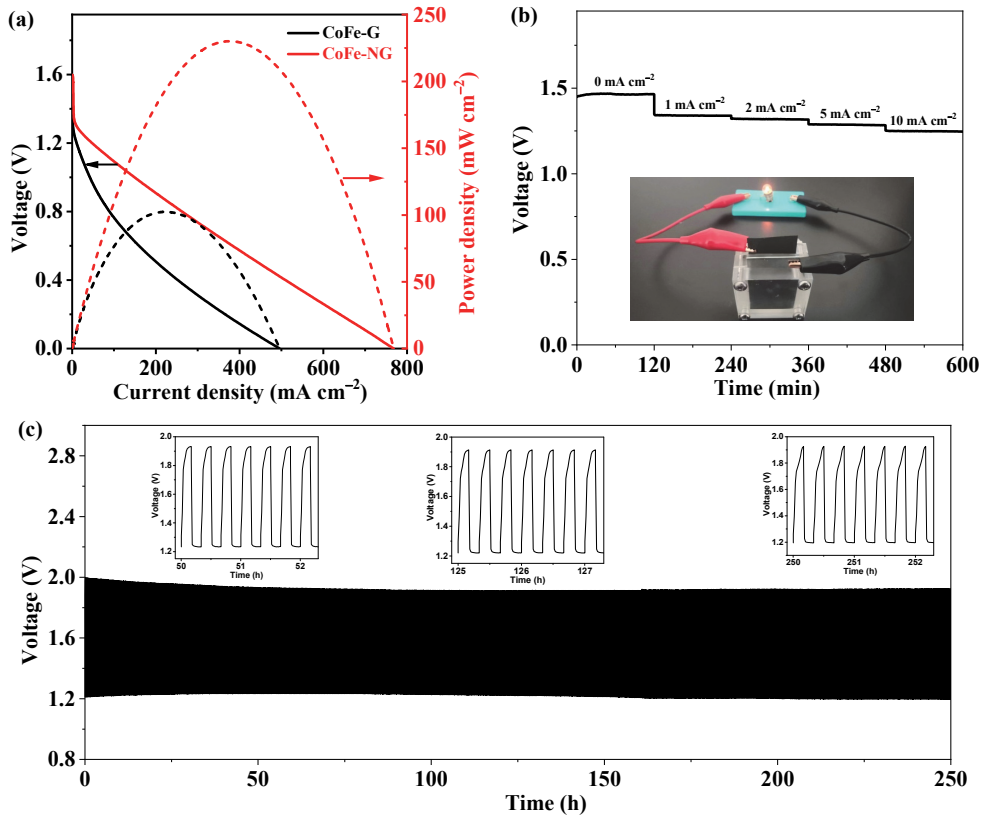

Fig. 5. (a) Polarization and power density curves of CoFe-NG-based and CoFe-G-based Zn-air batteries. (b) Discharge tests at different current densities of CoFe-NG-based battery. The inset is the digital picture of a small bulb powered by the CoFe-NG-based battery. (c) Galvanostatic discharge-charge cycling profiles of CoFe-NG-based battery at 5 mA cm^{-2}.

of 230 mW cm^{-2} (Fig. 5(a)), much higher than those of CoFe-G-based ZAB (1.4 V and 102 mW cm^{-2}), indicating that N-coordination to metal sites is an efficient means to enhance the battery performance. Moreover, the CoFe-NG-based ZAB affords stable galvanostatic discharge performance (Fig. 5(b)), which is very important for highly sensitive electronic devices and can successfully power a small bulb (the inset in Fig. 5(b)). Fig. 5(c) illustrates that CoFe-NG-based ZAB shows outstanding long-range cycling durability in discharge-charge processes, which might primarily be ascribed to the collaborative influence of Co-Fe dual sites in the CoFe-NG lowering the energy barrier for the electrode reaction.

3.4. Theoretical study

To confirm the microscopic kinetics of ORR process on the CoFe-NG dual-atom catalyst, the catalytic activity of the Fe-NG, Co-NG and CoFe-NG were elucidated by using DFT calculations. Firstly, the configurations of three intermediates on Fe-NG, Co-NG and CoFe-NG were optimized, as shown in Fig. 6(a). We found that OH or OOH group can be absorbed onto Fe sites spontaneously and the configuration could energetically favour to the catalytic process, which is consisted with the previous literature [42,43]. Fig. 6(a) illustrates the stable configurations of *OOH, *O, and *OH on the top or side view. In the first step (O_2 → *OOH), Co-NG and CoFe-NG are both endothermic and

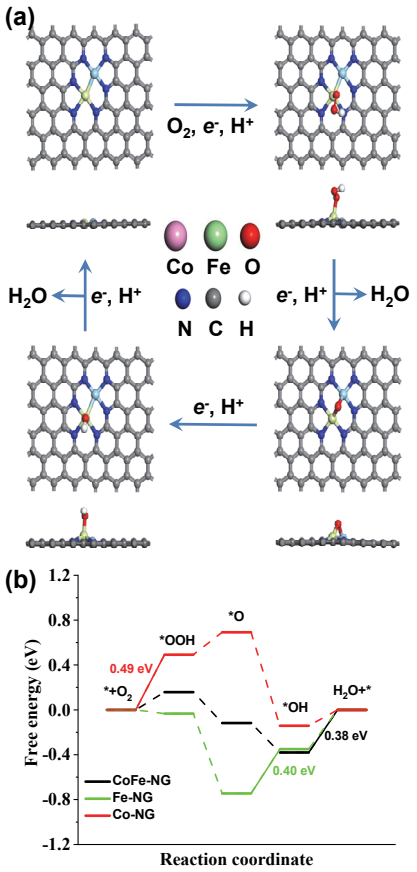

Fig. 6. (a) Top view and side view of the initial structures after absorbing *OOH, *O, and *OH on CoFe-NG. (b) Free energy diagram for the ORR of Fe-NG, Co-NG, and CoFe-NG at the potential of 1.23 V.

Co-NG shows the highest barrier of 0.49 eV, implying that the adsorption of O_2 is harder on CoN_4 and CoN_3-FeN_3 sites compare with FeN_4 site (Fig. 6(b)). For the step of *OOH → *O, there are no energy barriers for the reactions on CoFe-NG and Fe-NG except for Co-NG. However, Co-NG and CoFe-NG both exhibit lower energies in the third step of *O → *OH. Instead, Fe-NG shows a high barrier of 0.40 eV. Finally, the last step of *OH to H_2O on the three catalytic sites is an endothermic reaction. This result suggests that the three catalytic sites all present the excellent absorbability, especially for CoFe-NG with lower barrier of 0.38 eV. In addition, among the three intermediates, *OOH and *OH are bound to the Fe site, while *O favours to adsorb at the bridge site between Fe and Co, suggesting that the electronic interaction of intermediates with the metal sites and the configuration both play the critical role in the dual-atom ORR catalysis. In the ORR process, the highest potential barrier determines that the rate-limiting step on Fe-NG, Co-NG and CoFe-NG is *O → *OH (0.40 eV), O_2 → *OOH (0.49 eV), and *OH → H_2O (0.38 eV), respectively (Fig. 6(b)), demonstrating that the CoFe-NG could catalyse the ORR with the lowest energy barrier, which is in line with the experimental results.

4. Conclusions

In conclusion, we developed a novel dual-atom catalyst with FeN_3-CoN_3 sites on N-doped graphene nanosheets through one-pot annealing method. Benefiting from the synergic action of Fe and Co active sites, the CoFe-NG exhibited higher ORR activity than single-atom Fe-NG and Co-NG catalysts and Pt/C in the alkaline environment. The CoFe-NG-based Zn-air battery could afford a high peak power density of 230 mW cm^{-2} and exhibited negligible change in output voltage at 5 mA cm^{-2} for 250 h. DFT calculations suggested that FeN_3-CoN_3 sites exhibited lower energy barrier than FeN_4 and CoN_4 sites, and the rate-limiting step on the former is the transformation of *OH intermediate to H_2O, different from the transformation of *O to *OH on the FeN_4 site and the transformation of O_2 to *OOH on the CoN_4 site. This work will unfold a new window to devise high-performance dual-atom electrocatalysts for the ORR.

Electronic supporting information

Supporting information is available in the online version of this article.

Conflict of Interest

The authors declare no competing interests.

References

[1] S. Zhang, M. Chen, X. Zhao, J. Cai, W. Yan, J. C. Yen, S. Chen, Y. Yu, J. Zhang, *Electrochem. Energy Rev.*, **2021**, 4, 336–381.
[2] Q. Zhang, J. Guan, *Energy Environ. Mater.*, **2021**, 4, 307–335.
[3] Y. Fang, Y. Liu, L. Qi, Y. Xue, Y. Li, *Chem. Soc. Rev.*, **2022**, 51, 2681–2709.
[4] C. Huang, Y. Li, N. Wang, Y. Xue, Z. Zuo, H. Liu, Y. Li, *Chem. Rev.*,

2018, 118, 7744–7803.
[5] F. He, Y. Li, *CCS Chem.*, **2022**, DOI: 10.31635/ccschem.31022.202202328.
[6] D. Yuan, Y. Dou, Z. Wu, Y. Tian, K.-H. Ye, Z. Lin, S. X. Dou, S. Zhang, *Chem. Rev.*, **2022**, 122, 957–999.
[7] X. Wen, Q. Zhang, J. Guan, *Coord. Chem. Rev.*, **2020**, 409, 213214.
[8] Q. Zhang, J. Guan, *Nano Res.*, **2022**, 15, 38–70.
[9] L. Xiao, Z. Wang, J. Guan, *Coord. Chem. Rev.*, **2022**, 472, 214777.
[10] J. Guan, *J. Power Sources*, **2021**, 506, 230143.
[11] X. Bai, J. Guan, *Chin. J. Catal.*, **2022**, 43, 2057–2090.
[12] Q. Zhang, J. Guan, *Adv. Funct. Mater.*, **2020**, 30, 2000768.
[13] L. Hui, Y. Xue, H. Yu, Y. Liu, Y. Fang, C. Xing, B. Huang, Y. Li, *J. Am. Chem. Soc.*, **2019**, 141, 10677–10683.
[14] Y. Xue, B. Huang, Y. Yi, Y. Guo, Z. Zuo, Y. Li, Z. Jia, H. Liu, Y. Li, *Nat. Commun.*, **2018**, 9, 1460.
[15] H. Yu, Y. Xue, L. Hui, C. Zhang, Y. Fang, Y. Liu, X. Chen, D. Zhang, B. Huang, Y. Li, *Natl. Sci. Rev.*, **2021**, 8, nwaa213.
[16] Y. Gao, Y. Xue, F. He, Y. Li, *Proc. Natl. Acad. Sci. U. S. A.*, **2022**, 119, e2206946119.
[17] X. Zheng, Y. Xue, C. Zhang, Y. Li, *CCS Chem.*, **2022**, DOI: 10.31635/ccschem.31022.202202189.
[18] Y. Liu, Y. Gao, F. He, Y. Xue, Y. Li, *CCS Chem.*, **2022**, DOI: 10.31635/ccschem.31022.202202005.
[19] J. Han, J. Guan, *Chin. J. Catal.*, **2022**, DOI: 10.1016/S1872–2067(1022)64153–64156.
[20] F. Dong, M. Wu, Z. Chen, X. Liu, G. Zhang, J. Qiao, S. Sun, *Nano-Micro Lett.*, **2022**, 14, 36.
[21] H. Shen, E. Gracia-Espino, J. Ma, H. Tang, X. Mamat, T. Wagberg, G. Hu, S. Guo, *Nano Energy*, **2017**, 35, 9–16.
[22] Y. Lin, P. Liu, E. Velasco, G. Yao, Z. Tian, L. Zhang, L. Chen, *Adv. Mater.*, **2019**, 31, 1808193.
[23] Y. Wang, L. Wang, H. Fu, *Sci. China Mater.*, **2022**, 65, 1701–1722.
[24] S. Ma, G. A. Goenaga, A.V. Call, D.-J. Liu, *Chem. Eur. J.*, **2011**, 17, 2063–2067.
[25] X. Xie, C. He, B. Li, Y. He, D. A. Cullen, E. C. Wegener, A. J. Kropf, U. Martinez, Y. Cheng, M. H. Engelhard, M. E. Bowden, M. Song, T. Lemmon, X. S. Li, Z. Nie, J. Liu, D. J. Myers, P. Zelenay, G. Wang, G. Wu, V. Ramani, Y. Shao, *Nat. Catal.*, **2020**, 3, 1044–1054.
[26] T. Cui, Y.-P. Wang, T. Ye, J. Wu, Z. Chen, J. Li, Y. Lei, D. Wang, Y. Li, *Angew. Chem. Int. Ed.*, **2022**, 61, e202115219.
[27] C. Du, Y. Gao, H. Chen, P. Li, S. Zhu, J. Wang, Q. He, W. Chen, *J. Mater. Chem. A*, **2020**, 8, 16994–17001.
[28] S.-H. Yin, J. Yang, Y. Han, G. Li, L.-Y. Wan, Y.-H. Chen, C. Chen, X.-M. Qu, Y.-X. Jiang, S.-G. Sun, *Angew. Chem. Int. Ed.*, **2020**, 59, 21976–21979.
[29] F. Xiao, Q. Wang, G.-L. Xu, X. Qin, I. Hwang, C.-J. Sun, M. Liu, W. Hua, H.-w. Wu, S. Zhu, J.-C. Li, J.-G. Wang, Y. Zhu, D. Wu, Z. Wei, M. Gu, K. Amine, M. Shao, *Nat. Catal.*, **2022**, 5, 503–512.
[30] L. Zhang, J. M. T. A. Fischer, Y. Jia, X. Yan, W. Xu, X. Wang, J. Chen, D. Yang, H. Liu, L. Zhuang, M. Hanke, D. J. Searles, K. Huang, S. Feng, C. L. Brown, X. Yao, *J. Am. Chem. Soc.*, **2018**, 140, 10757–10763.
[31] J. Wang, Z. Huang, W. Liu, C. Chang, H. Tang, Z. Li, W. Chen, C. Jia, T. Yao, S. Wei, Y. Wu, Y. Li, *J. Am. Chem. Soc.*, **2017**, 139, 17281–17284.
[32] Z. Lu, B. Wang, Y. Hu, W. Liu, Y. Zhao, R. Yang, Z. Li, J. Luo, B. Chi, Z. Jiang, M. Li, S. Mu, S. Liao, J. Zhang, X. Sun, *Angew. Chem. Int. Ed.*, **2019**, 58, 2622–2626.
[33] J. Huang, L. Sementa, Z. Liu, G. Barcaro, M. Feng, E. Liu, L. Jiao, M. Xu, D. Leshchev, S.-J. Lee, M. Li, C. Wan, E. Zhu, Y. Liu, B. Peng, X. Duan, W. A. Goddard, III, A. Fortunelli, Q. Jia, Y. Huang, *Nat. Catal.*, **2022**, 5, 513–523.
[34] H. Kresse, *Phys. Rev. B*, **1993**, 47, 558–561.
[35] H. Kresse, *Phys. Rev. B*, **1994**, 49, 14251–14269.
[36] F. Li, Y. Bu, G.-F. Han, H.-J. Noh, S.-J. Kim, I. Ahmad, Y. Lu, P. Zhang,

Graphical Abstract

Chin. J. Catal., 2023, 46: 48–55 doi: 10.1016/S1872-2067(22)64189-5

Dual-atom Co-Fe catalysts for oxygen reduction reaction

Tianmi Tang, Yin Wang, Jingyi Han, Qiaoqiao Zhang, Xue Bai, Xiaodi Niu *, Zhenlu Wang, Jingqi Guan *
Jilin University; Inner Mongolia Minzu University

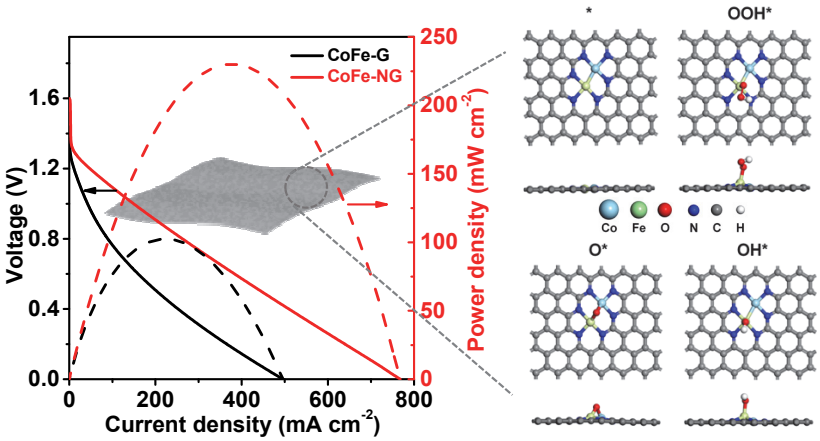

Dual-atom Co-Fe catalysts exhibit excellent ORR performance due to the synergistic effect of Co-Fe dual-sites in the CoFe-NG lowering the energy barrier for the ORR, which can be assembled into zinc-air batteries as air-cathode catalysts, delivering a high peak power density of 230 mW cm^{-2}.

H.Y. Jeong, Z. Fu, Q. Zhong, J.-B. Baek, *Nat. Commun.*, **2019**, 10, 2623.
[37] X. Bai, L. Wang, B. Nan, T. Tang, X. Niu, J. Guan, *Nano Res.*, **2022**, 15, 6019–6025.
[38] P. Yin, T. Yao, Y. Wu, L. Zheng, Y. Lin, W. Liu, H. Ju, J. Zhu, X. Hong, Z. Deng, G. Zhou, S. Wei, Y. Li, *Angew. Chem. Int. Ed.*, **2016**, 55, 10800–10805.
[39] Y. Han, H. Duan, C. Zhou, H. Meng, Q. Jiang, B. Wang, W. Yan, R. Zhang, *Nano Lett.*, **2022**, 22, 2497–2505.
[40] W. Zhu, Y. Pei, J. C. Douglin, J. Zhang, H. Zhao, J. Xue, Q. Wang, R. Li, Y. Qin, Y. Yin, D. R. Dekel, M. D. Guiver, *Appl. Catal. B*, **2021**, 299, 120656.
[41] K. Wang, J. Liu, Z. Tang, L. Li, Z. Wang, M. Zubair, F. Ciucci, L. Thomsen, J. Wright, N. M. Bedford, *J. Mater. Chem. A*, **2021**, 9, 13044–13055.
[42] M. Xiao, L. Gao, Y. Wang, X. Wang, J. Zhu, Z. Jin, C. Liu, H. Chen, G. Li, J. Ge, Q. He, Z. Wu, Z. Chen, W. Xing, *J. Am. Chem. Soc.*, **2019**, 141, 19800–19806.
[43] X. Zhao, X. Liu, B. Huang, P. Wang, Y. Pei, *J. Mater. Chem. A*, **2019**, 7, 24583–24593.

用于氧还原反应的双原子钴-铁催化剂

唐甜蜜[a,1], 王　寅[c,1], 韩憬怡[a], 张巧巧[a], 白　雪[a], 牛效迪[b,*], 王振旅[a], 管景奇[a,*]
[a]吉林大学化学学院, 物理化学研究所, 吉林长春130021
[b]吉林大学食品科学与工程学院, 吉林长春130062
[c]内蒙古民族大学化学与材料学院, 内蒙古自治区纳米碳材料重点实验室, 纳米创新研究院, 内蒙古通辽028000

摘要: 金属-空气电池因其高效率和便携性受到广泛关注. 然而, 氧还原反应(ORR)的高能垒和缓慢的动力学导致其输出功率低. 尽管贵金属铂基材料具有较高的ORR活性, 但其在工业上的大规模应用受到高成本的制约. 因此, 迫切需要以储量丰富的非贵金属为原料, 开发具有低成本、高性能和耐用性的催化剂. 近年来, 单原子过渡金属与氮共掺杂碳材料(M-N-C)成为替代贵金属催化剂的理想材料. 理论模拟和实验结果均表明, 单原子Fe/Co-N-C催化剂具有良好的ORR活性, 其中FeN_4和CoN_4构型被认为是主要活性位点. 此外, 含有相邻金属位点的双金属单原子催化剂具有加速ORR动力学的巨大潜力. 通过对ORR中间体的桥式-顺式吸附, 双金属位点可以促进O–O键的裂解, 从而提高催化活性. 除固有活性外, 双金属位点可减少ORR过程中含氧中间体对M–N键的攻击, 提高M-N-C对ORR的耐久性和工业应用潜力. 因此, 近年来, 研究者开始探索双金属单原子催化剂的合成和电催化性能, 发现Fe-Co, Fe-Mn, Fe-Cu, Co-Zn和Co-Pt双位点可以有效催化ORR.

为进一步提高ORR活性, 需要合理调节双原子结构, 并引入更多的双金属位点. 本文在氮掺杂石墨烯纳米片上构建了一种含FeN_3-CoN_3位点的新型双原子催化剂(CoFe-NG), 该催化剂具有较好的ORR催化活性, 半波电位为0.917 V, Tafel斜率为46 mV dec^{-1}, 远远优于单原子Fe-NG、单原子Co-NG和Pt/C催化剂. Koutecky-Levich曲线和H_2O_2产率揭示了CoFe-NG具有高效的四电子ORR过程, 不仅表现出高电流密度, 而且对氧还原为OH^-(而不是过氧化氢)更具选择性. 计时安培测试结果表明, CoFe-NG对甲醇和一氧化碳中毒具有较高的耐受性. KSCN中毒实验结果表明, SCN^-离子与Fe和Co位点发生强配位作用并使活性位点中毒. 以CoFe-NG为空气电极组装的锌-空气电池, 开路电压为1.47 V, 峰值功率密度高达230 mW cm^{-2}, 具有良好的充放电循环稳定性, 可以为一个小灯泡供电, 并且在5 mA cm^{-2}条件下持续充放电250 h, 输出电压几乎不变. 理论计算表明, 掺氮石墨烯上的FeN_3-CoN_3位点比FeN_4和CoN_4位点具有更低的ORR能垒, FeN_3-CoN_3位点上的速控步是*OH中间体向H_2O的转化, 与单位点FeN_4和CoN_4不同. 综上, 本文为可控合成高性能双金属单原子催化剂及进一步深入分析其电催化氧还原反应机理提供参考.

关键词: 双原子催化剂; M-N-C; 氧还原反应; 理论计算; 锌-空气电池

收稿日期: 2022-09-11. 接受日期: 2022-10-24. 上网时间: 2023-03-05.
*通讯联系人. 电子信箱: niuxd@jlu.edu.cn (牛效迪), guanjq@jlu.edu.cn (管景奇).
[1]共同第一作者.
基金来源: 国家自然科学基金(22075099); 吉林省自然科学基金(20220101051JC); 吉林省教育厅项目(JJKH20220967KJ, JJKH20220968CY).